Check for updates

ADVANCED MATERIALS
www.advmat.de

Embedded 3D Printing of Architected Ceramics via Microwave-Activated Polymerization

*Benito Román-Manso, Robert D. Weeks, Ryan L. Truby, and Jennifer A. Lewis**

Light- and ink-based 3D printing methods have vastly expanded the design space and geometric complexity of architected ceramics. However, light-based methods are typically confined to a relatively narrow range of preceramic and particle-laden resins, while ink-based methods are limited in geometric complexity due to layerwise assembly. Here, embedded 3D printing is combined with microwave-activated curing to generate architected ceramics with spatially controlled composition in freeform shapes. Aqueous colloidal inks are printed within a support matrix, rapidly cured via microwave-activated polymerization, and subsequently dried and sintered into dense architectures composed of one or more oxide materials. This integrated manufacturing method opens new avenues for the design and fabrication of complex ceramic architectures with programmed composition, density, and form for myriad applications.

1. Introduction

There is growing interest in using additive manufacturing methods to produce geometrically complex ceramics[1,2] for myriad applications, including catalyst supports,[3,4] battery electrodes,[5,6] heat exchangers,[7] and bone scaffolds,[8–12] among others. Currently, stereolithography[13–19] (SLA) and direct ink writing[20–25] (DIW) are the most widely used methods for printing ceramic structures. Ceramic-based SLA relies on the photopolymerization of preceramic polymers[17,26] or particle-laden resins.[27] Preceramic polymer resins have been used to produce silicon oxycarbide (SiOC) or oxynitride (SiON) structures, while particle-laden SLA resins may result in a wider range of ceramic materials. However, particle fillers can hinder photopolymerization if their refractive index differs from that of the base photopolymerizable resin leading to reduced feature resolution and build speed.[28] Such resins must also exhibit low viscosity to enable their flow into thin layers during SLA printing, which often limits their particle loading[13,15] and, consequently, their final density. By contrast, DIW is an extrusion-based 3D printing (3DP) method that is well suited for patterning concentrated colloidal gels,[21,23,29,30] preceramic polymers,[31,32] and foams[33–35] in a layerwise manner. To date, DIW has been used to produce periodic ceramic architectures ranging from honeycombs to 3D woodpile lattices. However, despite significant advances in both light- and ink-based 3DP methods, freeform fabrication of ceramic architectures with arbitrary composition and geometry remains challenging.

Embedded 3D (EMB3D) printing offers a promising route for creating architected ceramics via freeform writing in a support matrix. In its initial embodiment, vascularized systems were produced by writing sacrificial inks within soft[36,37] and living[38] matrices. This method was extended to create soft strain sensors and proprioceptive robotic grippers by writing conductive particle-filled[39] and ionogel inks[40] within elastomeric matrices, respectively. More recently, other research groups have generated ceramic filaments by printing colloidal inks within a sacrificial support matrix.[41,42] However, they did not create complex structures nor report their microstructural or mechanical properties after densification. Hence, the ability to dry, cure, and harvest ceramic parts produced by EMB3D printing for load-bearing applications has yet to be demonstrated.

Here, we report a method for fabricating architected ceramics with controlled composition in arbitrary geometries that combines EMB3D printing with microwave-activated curing.[43,44] We first created concentrated colloidal gels that contain thermally curable species and are compatible with our silicone-based support matrix while exhibiting the requisite rheological properties for EMB3D printing. As exemplars, we printed architected ceramics in the form of monolithic and multimaterial lattices, as well as interpenetrating chain structures. Next, we investigated the effects of microwave-activated curing on the ability to generate parts with sufficient handling strength for their removal from the support matrix and subsequent densification during sintering. Our integrated manufacturing approach enables complex ceramics architectures to be manufactured with programmable composition in freeform shapes that may be of potential interest for structural, biomedical, and energy applications.

2. Results and Discussion

EMB3D printing with microwave-activated curing is shown in **Figure 1**a. Printed filaments are extruded through a nozzle

B. Román-Manso, R. D. Weeks, R. L. Truby, J. A. Lewis
John A. Paulson School of Engineering and Applied Sciences
and the Wyss Institute for Biologically Inspired Engineering
Harvard University
Cambridge, MA 02138, USA
E-mail: jalewis@seas.harvard.edu

The ORCID identification number(s) for the author(s) of this article can be found under https://doi.org/10.1002/adma.202209270.

DOI: 10.1002/adma.202209270

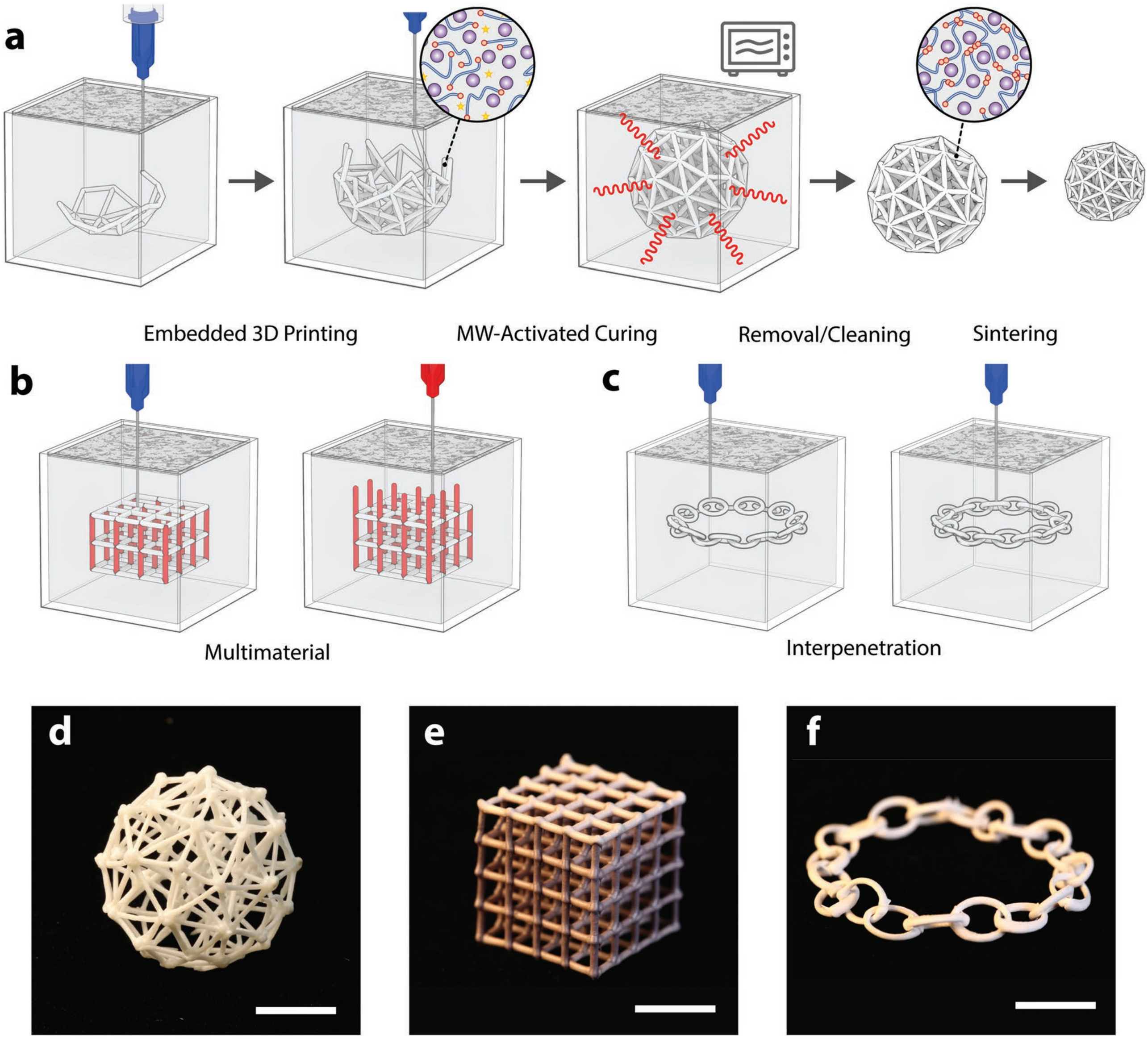

Figure 1. Microwave-activated, EMB3D printing of architected ceramics. a) Schematic illustration of the process workflow for EMB3D printing of ceramic lattices. b) Schematic illustration of EMB3D printing of multimaterial ceramic lattices. c) Schematic illustration of EMB3D printing of interpenetrating (chainmail) architecture. d–f) Optical images of printed YSZ architectures: d) stochastic sphere, e) multimaterial lattice composed of pure (horizontal) and cobalt-doped (vertical) YSZ struts, and f) interpenetrating ceramic links patterned in the form of a closed chain. Scale bars: (d–f) = 15 mm.

that is translated within a self-healing, silicone support matrix. Print paths for complex architectures are generated either using Automated Eulerian Route Optimization (AERO)[45] or manually. After printing, each ceramic architecture is exposed to microwave irradiation to induce rapid thermal curing of the embedded colloidal ink(s). Using this approach, we can decouple the drying and curing processes, which typically occur simultaneously during conventional heating resulting in large surface and internal cracks (Figure S1, Supporting Information). The printed and cured ceramic architectures are sufficiently robust to withstand capillary-induced drying stresses that drive crack formation.[46,47] Microwave-activated curing also minimizes the temperature gradients that lead to regions of non-uniform thermal expansion within the silicone support matrix, which arise during conventional heating. After curing, these objects are strong enough to be removed from the silicone matrix for subsequent cleaning, drying, and sintering steps. Two or more inks can be sequentially printed through separate nozzles via EMB3D printing to generate multimaterial structures, such as lattices where vertical and horizontal struts are composed of different materials (Figure 1b). This method can also be used to print interpenetrated ceramic features, such as chain links that move independently from one another (Figure 1c). Several representative ceramic architectures have been produced as exemplars, including an yttria-stabilized zirconia (YSZ) stochastic sphere (Figure 1d), a multimaterial lattice produced by coprinting with vertical struts composed of cobalt oxide (CoO)-doped YSZ and pure YSZ horizontal struts

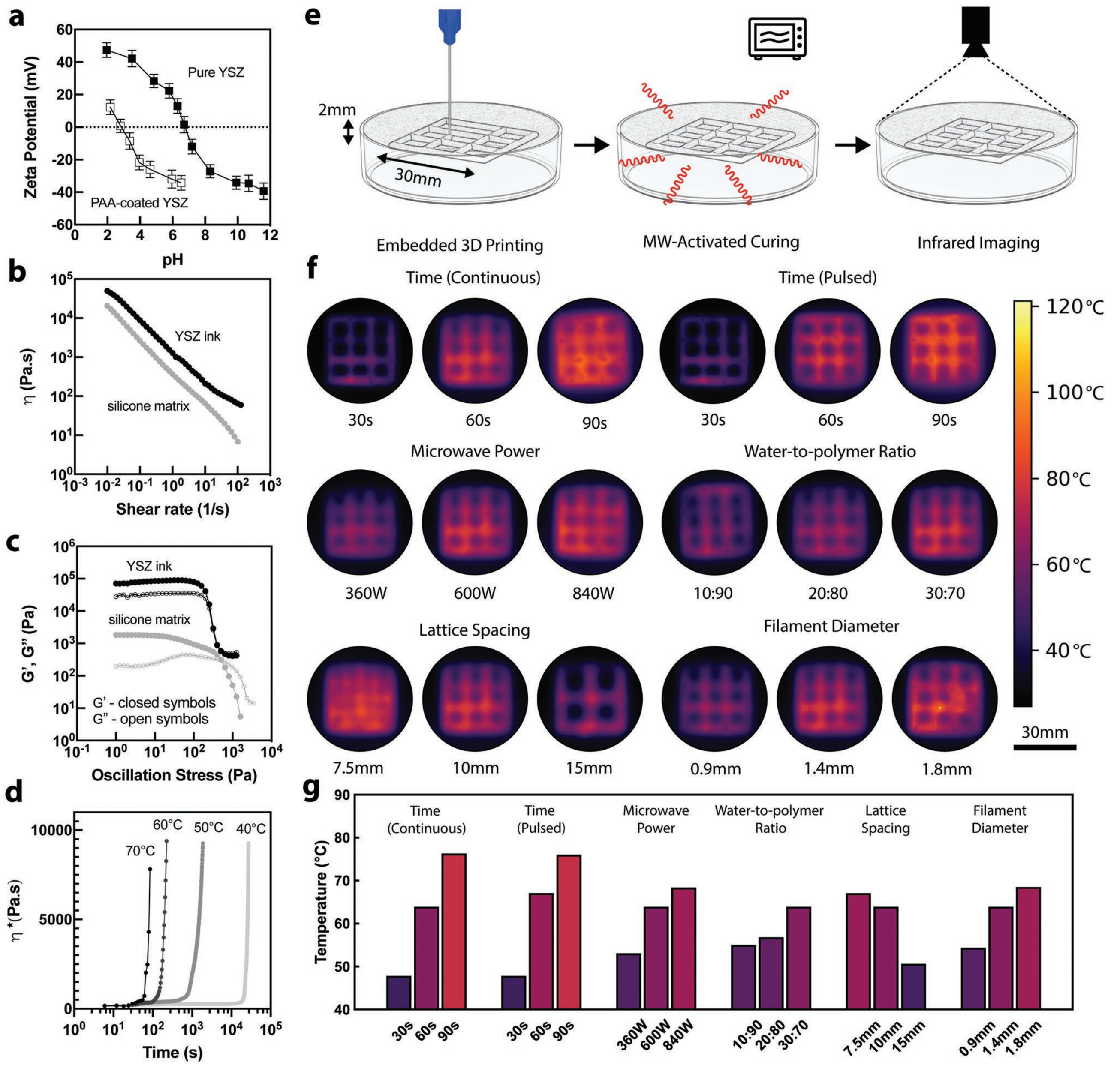

Figure 2. Optimization of ink, matrix, and microwave-activated curing conditions. a) Zeta potential as a function of pH for pure and PAA-coated YSZ particles. b) Apparent viscosity as a function of shear rate and c) storage (G') and loss modulus (G'') as a function of oscillation stress, for the pure YSZ ink and silicone matrix. d) Complex viscosity, η^*, as a function of curing time of pure YSZ inks held at different temperatures. e) Schematic workflow for printing, microwave-activated curing, and thermal imaging of 2D ceramic lattices. f) Thermal surface maps of the YSZ lattices embedded in a silicone matrix, which highlight the effects of irradiation parameters, ink composition, and lattice geometry on curing. g) Average surface temperature measured for the parameters shown in (f).

(Figure 1e), and a YSZ chain structure (Figure 1f). EMB3D printing can be easily parallelized using multiple printheads mounted to a single motion stage to significantly increase throughput (Figure S2, Supporting Information).

Viscoelastic colloidal inks are created for EMB3D printing by suspending YSZ particles, and dissolving a poly(acrylic acid) (PAA) dispersant, a cross-linkable poly(ethylene glycol) diacrylate (PEGDA 700), and a thermal initiator, 4,4′-azobis(4-cyanopentanoic acid) (ACPA) in water at a pH of 5.5–6, which is above the isoelectric point of the PAA-stabilized YSZ particles (**Figure 2**a). The resulting YSZ particle gel exhibits strong shear thinning behavior (Figure 2b) and an apparent viscosity that is roughly three-fold higher than that of the silicone support matrix over the broad range of shear rates explored. As reported previously, when the ink and matrix viscosities are within an order of magnitude, cylindrical filaments can be readily printed with good connectivity at the nodes.[45] These inks flow once their characteristic shear yield stress, τ_y, of ≈300 Pa is exceeded. However, the inks exhibit a solid-like response, i.e., their storage modulus ($G' \approx 10^5$ Pa) exceeds their loss modulus (G'')

in the linear elastic regime, allowing them to retain their cylindrical features under quiescent conditions (Figure 2c). Similar behavior is observed for the silicone support matrix, which has a lower plateau G' of ≈2×10^3 Pa and a higher shear yield stress, τ_y, of ≈500 Pa.

To probe their curing kinetics, YSZ inks are heated to different temperatures, held isothermally, and their complex viscosity (η*) is measured as a function of curing time. For each temperature evaluated, two distinct polymerization regimes are observed (Figure 2d). In the first regime (*R1*), η* gradually rises over time due to the formation of initial cross-links between individual PEGDA chains. In the second regime *(R2)*, η* exhibits an asymptotic rise as rapid chain growth occurs ultimately producing a space-filling polymer network (Figure S3a, Supporting Information). The inflection point at the $R1 \rightarrow R2$ transition, which is defined by the intersection of lines fitted to each regime, occurs at η* ≈500 Pa s for all temperatures evaluated. We posit that the thermal decomposition kinetics of the APCA initiator dictates the characteristic curing time, t_c, associated with polymer network formation (Figure S3b, Supporting Information), which is defined by the time at which η* reaches ≈5000 Pa s for each temperature. Using the curing kinetics model outlined in Supporting Information, we find that the experimentally determined values of t_c for the YSZ-based ink range from ≈7 h at 40 °C to 1 min at 80 °C (Table S1, Supporting Information). The measured values are in good agreement with those predicted using the known thermal decomposition rate, K_d, of the ACPA initiator,[48] where t_c is inversely proportional to K_d at each temperature.

Next, we directly assess the respective contributions of several parameters that may influence the kinetics of microwave-activated curing of the printed features. After printing 2D YSZ lattices within the silicone support matrix, the lattice-containing matrix system is subjected to microwave irradiation and the resulting temperature distributions are measured by infrared imaging (Figure 2e). Unless otherwise noted, the standard experimental conditions for this study are defined as follows: 60 s irradiation time, 600 W irradiation power (continuous mode), 30:70 water-to-polymer volume ratio, 10 mm center-to-center separation distance between struts within the printed lattices, and 1.4 mm strut diameter. When these lattices are subjected to different microwave irradiation times (30, 60, and 90 s), the corresponding thermal maps reveal: (i) in situ heating of the printed filaments due to the presence of water in these inks and (ii) increasing temperature as a function of irradiation time (Figure 2f). Since silicone possesses low thermal conductivity, heat diffusion from the embedded lattices to the surrounding support matrix is limited. Consequently, microwave irradiation at higher irradiation power of 1200 W results in temperatures exceeding 100 °C (the boiling point of water), inducing rapid bubble formation within the printed lattices (Figure S4 and Movie S1, Supporting Information) and, hence, large microstructural defects (Figure S5, Supporting Information). By controlling the total microwave irradiation power and duration as well as implementing an on/off pulsed sequence (Figure S6), a more uniform temperature distribution is achieved with maximum temperatures that are sufficient for rapid thermal curing, yet remain below 100 °C (Figure S7, Supporting Information). When the printed and embedded 2D lattices are subjected to a total irradiation time of 30 s, 60 s, and 90 s using 1, 2, or 3 pulses, respectively, lattice average temperatures reveal that negligible heat dissipation occurs during off intervals (Figure 2g). We quantitatively compare thermal maps of the entire circular dish (including both lattice and matrix) by analyzing their associated histograms (pixel count as a function of different temperature ranges) as shown in Figure S6 (Supporting Information). Notably, after 90 s of microwave irradiation, the temperature distribution in the pulsed mode is slightly more homogeneous than that observed for the continuous mode, suggesting that some heat from the lattice has dissipated into the matrix. Next, lattices are printed from YSZ inks of varying water-to-polymer volume ratios (10:90, 20:80, 30:70). Printed lattices with the highest water content exhibited higher average temperatures during microwave curing (Figure 2g). Finally, the effects of the lattice geometry are probed by varying either the center-to-center separation distance between printed struts or the strut diameter. During microwave-activated curing, 2D lattices with decreasing spacing between struts or larger strut diameters exhibit larger temperature increases, with temperatures exceeding 100 °C for printed lattices composed of the largest struts (1.8 mm in diameter, Figure S7, Supporting Information).

Microwave-activated curing must be optimized to minimize (and ideally eliminate) defects, such as surface spallation, cracking, or bubble formation (Figure S1 and Movie S1, Supporting Information). Toward this goal, we printed four octet unit cells composed of YSZ inks containing either a 10:90 or 30:70 water-to-polymer volume ratio, which were cured at microwave powers of either 360 W or 600 W. Micro-CT scans of the cross-sections of individual struts reveal the presence of striations within these printed and cured unit cells. These features are more abundant for octet unit cells printed from inks with a 10:90 water-to-polymer ratio and subjected to higher microwave power (**Figure 3**a; microwave power of 360 W in Movie S2, Supporting Information and 600 W in Movie S3, Supporting Information). These octet unit cells are subsequently heated to 500 °C for 2 h to remove the polymeric species followed by sintering at 1500 °C for 2 h to promote densification. Micro-CT scans of the cross-sections of individual sintered struts reveal that catastrophic crack formation occurs in unit cells printed from YSZ inks with a 10:90 water-to-polymer ratio. By contrast, unit cells printed from YSZ inks with a higher 30:70 water-to-polymer ratio exhibit a marked reduction in these defects. We theorize that the cracking phenomena for inks with lower water contents arise due to internal stresses developed during the formation of a stiffer network of covalent polymer bonds as water vapor diffuses away from each strut. Importantly, nearly crack-free struts are attained with the 30:70 water-to-polymer inks when cured more slowly using a microwave power of 360 W (Movie S4, Supporting Information) compared to 600 W (Movie S5, Supporting Information). Micro-CT scans of a full octet unit cell are shown in Figures 3b–g, demonstrating the absence of catastrophic cracks splitting individual struts. A scanning electron microscopy (SEM) image of a representative node from a cubic YSZ lattice is shown to illustrate the outer sphericity of the joint between two or more struts (Figure 3h). Notably, upon sintering, these YSZ structures achieve 97% of their theoretical density. Representative images of cured and sintered

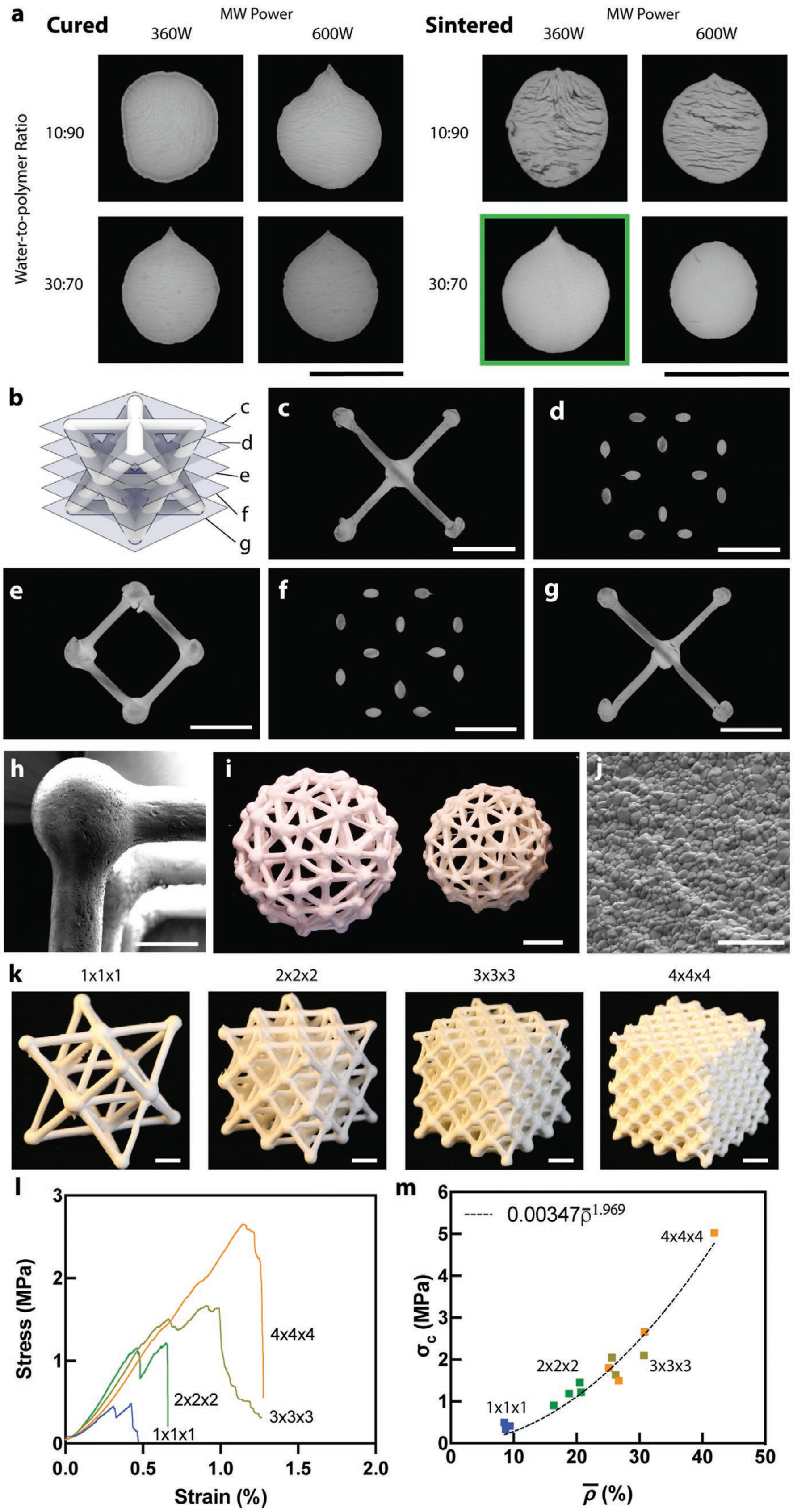

Figure 3. Microstructural evolution and mechanical properties of sintered ceramic architectures. a) Micro-CT images of strut cross-sections, which show the effects of ink composition (i.e., water-to-polymer ratio) and microwave power on defect formation. b) Schematic view of a unit cell within an

YSZ spherical lattices indicated that these structures undergo a linear shrinkage of ≈23% during sintering (Figure 3i). A high-resolution SEM image of a fractured YSZ sintered strut is shown in Figure 3j, which reveals a highly uniform, dense microstructure that consists of YSZ grains with an average size of 0.6 – 0.7 µm.

We characterized the mechanical properties of the embedded printed, cured, and sintered ceramic architectures by carrying out compression tests on YSZ octet structures. Four types of YSZ octet lattices with $1 \times 1 \times 1$, $2 \times 2 \times 2$, $3 \times 3 \times 3$, and $4 \times 4 \times 4$ unit cells per structure are fabricated (Figure 3k) with respective relative density ($\bar{\rho}$) values of 8.5–9.5%, 16.5–21%, 25.5–31% and 25–42%. The range of $\bar{\rho}$ values for each lattice type arises primarily from differences in their printed strut diameter due to slight batch-to-batch variations in ink viscosity. We note that some $4 \times 4 \times 4$ lattices are printed with smaller strut diameters to enable EMB3D printing without crossing over previously patterned features; thus, the $\bar{\rho}$ ranges for $3 \times 3 \times 3$ and $4 \times 4 \times 4$ lattices overlap. The stress-strain behavior observed for representative octet lattices under compression is shown in Figure 3l and accompanying Movies S6–S9 (Supporting Information), respectively. Linear deformation is observed during their initial loading, which results in similar effective Young's modulus of $\tilde{E} \approx$ 270–280 MPa. We observed that one or more struts fracture in $1 \times 1 \times 1$, $2 \times 2 \times 2$, and $3 \times 3 \times 3$ lattices at strains under 1%. This first fracture event can lead to catastrophic failure in some cases, where the maximum load corresponds to an effective compressive strength (σ_c). For other lattices, fracture of a single strut leads to a sudden drop in the stress-strain curve, which then recovers to σ_c before failing catastrophically. The measured σ_c values range from 0.4 MPa for low density ($1 \times 1 \times 1$) lattices to ≈5 MPa for high density ($4 \times 4 \times 4$) lattices and scale roughly with their relative density as $\sigma_c \propto \bar{\rho}^{1.97}$ (Figure 3m). We note that both the effective Young's modulus and the compressive strength should theoretically scale linearly with the relative density for ideal stretching-dominated (octet) lattices.[49] We attribute this discrepancy to the small number of unit cells (< ≈7 cells) that make up the lattices used for compressive testing, which result in significant edge effects. Nonetheless, these tests demonstrate the mechanical robustness of ceramic lattices produced by microwave-assisted EMB3D printing.

As a final demonstration, we created interpenetrating ceramics in the form of chain-like structures (**Figure 4**). A small YSZ chain consisting of 12 round links is rapidly heated with a propane torch while holding a 200 g weight, until a temperature of ≈1000 °C is reached on the chain surface (Figure 4a). The chain maintains its structural integrity during and after the test (see Movie S10, Supporting Information). In addition, Figure 4b shows a tensile measurement carried out on a representative YSZ chain loop comprised of 20 round links with an outside link diameter of 10 mm, filament diameter of 1.75 mm and an average weight per link of 0.4 g. The representative force–displacement curve exhibits an approximately linear slope until the weakest link fails catastrophically (Movie S11, Supporting Information). To highlight the versatility of EMB3D printing, we created a multimaterial architecture in the form of a Japanese 4-1 chainmail weave composed of discrete links arranged in a graded fashion from Ni-doped alumina (cyan) to YSZ (white), as shown in Figure 4c. This interpenetrating architecture is printed in three steps (Figure 4d, Movie S12, Supporting Information). First, the bottom halves of rings are printed, starting with the Ni-doped alumina, and finishing with the YSZ rings. Second, whole rings are printed in the x–y plane, one material at a time. Finally, the top halves of the rings are printed to close the chainmail. Next, the chainmail architecture is subjected to microwave curing (360 W, 4 cycles of 30 s on/off pulses) followed by polymer removal (500 °C, 2 h) and sintering (1500 °C, 2 h). Importantly, we find that the discrete links within these interpenetrating structures do not fuse together during the sintering process, even when the chain is bundled up. We note that creating complex objects with freely moving elements composed of multiple materials using light-based 3DP methods has remained elusive. We envision other classes of materials with vastly different mechanical properties which could be combined within interpenetrating structures to create lightweight or smart fabrics with remarkable properties.[50]

3. Conclusion

We have demonstrated a microwave-activated EMB3D printing method for creating complex ceramic architectures in both monolithic and multimaterial motifs. We have created inks with optimized composition and rheology for a chemically compatible support matrix and used EMB3D printing to achieve a new level of geometric complexity for ceramic parts. We have shown that microwave-activated thermal curing enables the fabrication of lightweight ceramic lattices and interpenetrating chainmail structures. The ability to rapidly print and microwave cure particle-filled, polymeric materials opens new avenues for generating architected matter ranging from ceramics to lightweight polymer composites and fabrics.

4. Experimental Section

Colloidal Inks: Three different colloidal inks were produced: (i) pure YSZ ink, (ii) a cobalt (II) oxide (CoO)-doped YSZ ink and (iii) a nickel (II) oxide (NiO)-doped alumina (Al_2O_3) ink. For the YSZ inks, a stock solution was prepared first containing poly(ethylene glycol) (PEG 4*k* with a molecular weight of 4000 g mol^{-1}, EMD Millipore; PEG 20*k*, with a molecular weight of 20 000 g mol^{-1}, Sigma) dissolved in deionized water. Next, the poly(ethylene glycol) diacrylate (PEGDA 700, Sigma) was added, which serves as a cross-linkable monomer, and poly(acrylic acid) (PAA M_w ≈1800, Sigma), which serves as a dispersant. A small amount of nitric acid (HNO_3, Sigma) was then added to adjust

octet lattice, denoting the cross-sections analyzed in micro-CT scans of struts. c–g) Micro-CT images of a single unit cell in a YSZ octet lattice, printed using an ink composed of a 30:70 water-to-polymer ratio and cured at 360 W using four (30 s) on/off cycles. h) SEM image of a single node within a YSZ lattice. i) Printed (left) and sintered (right) YSZ domes. j) SEM image of sintered YSZ microstructure. k) 3D-printed, sintered YSZ octet lattices with $1 \times 1 \times 1$, $2 \times 2 \times 2$, $3 \times 3 \times 3$, and $4 \times 4 \times 4$ unit cells. l) Representative compressive stress–strain curves for the lattices in (k). l) Compressive strength, σ_C, as a function of relative density, $\bar{\rho}$, for lattices of varying density. Scale bars: (a) = 1 mm, (c–g) = 5 mm, (h) = 1 mm, (i) = 10 mm, (j) = 5 µm, (k) = 5 mm.

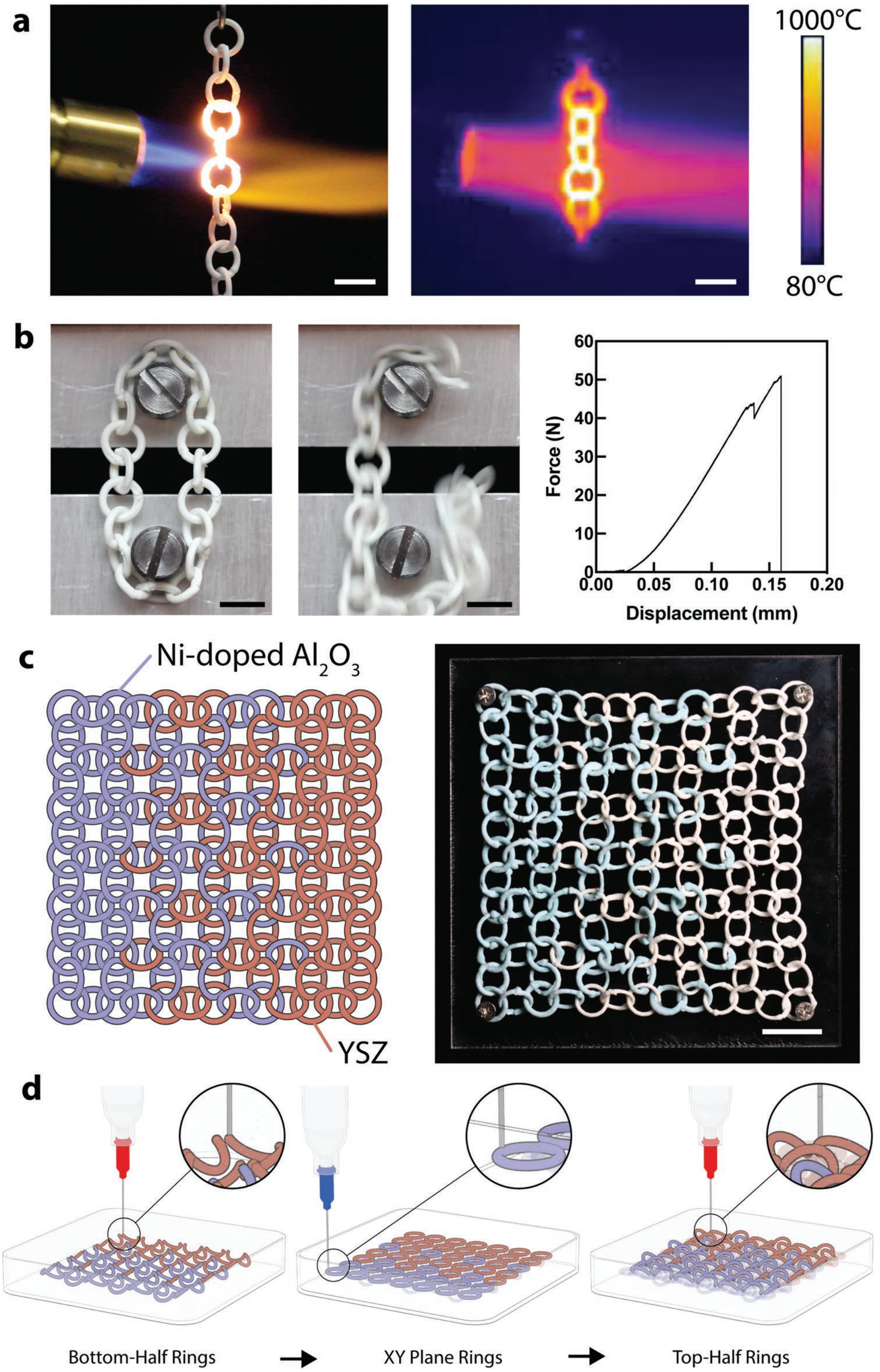

Figure 4. EMB3D printing of interpenetrating ceramic architectures. a) Conventional and infrared image of a ceramic chain heated to 1000 °C. b) Images of tensile testing and fracture behavior of a ceramic chain loop, where the applied force as a function of displacement is plotted. c) Diagram and optical image of a compositionally graded chainmail composed of Ni-doped Al_2O_3 (blue) and YSZ (white) links. d) Schematic workflow process for EMB3D printing of multimaterial interpenetrated chainmail structures. All scale bars = 10 mm.

the pH 5–5.6. The final stock solution contained 72.63 wt% PEGDA, 22.64 wt% water, 4.1 wt% PAA, 0.53 wt% HNO_3, 0.05 wt% PEG 4*k*, and 0.05 wt% PEG 20*k*. The stock solution was mixed at 2000 rpm for 20 s in a planetary mixer (SpeedMixer DAC 600.2; FlackTek, Inc). Submicrometer-sized YSZ powder (Sigma, 464228) is added to this stock solution in a stepwise fashion (≈6 steps). Following each step, the ink was homogenized at 2000 rpm for 30 s in the planetary mixer. Once the final amount of YSZ powder has been added, the ink was mixed at 2000 rpm for 60 s prior to adding a thermal initiator (4,4′-azobis (4-cyanopentanoic acid), ACPA (Sigma), which is pre-dissolved in water. The ink is mixed at 1500 rpm for 30 s following the two-step addition of thermal initiator and then stored at 5–8 °C until needed for printing. The final ink contained 79.61 wt% YSZ, 13.8 wt% PEGDA, 5.28 wt% water, 0.78 wt% PAA, 0.41 wt% ACPA, 0.1 wt% HNO_3, 0.01 wt% PEG 4*k*, and 0.01 wt% PEG 20*k*, which corresponded to an YSZ volume fraction of $\phi \approx 0.41$. The CoO-doped YSZ ink was prepared following the same procedure, except that 1 wt% YSZ powder was replaced by 1 wt% CoO powder (Sigma).

The NiO-doped Al_2O_3 ink was prepared following a nearly identical procedure, starting with a stock solution composed of PEGDA 700 (Sigma, 455 008), ammonium polyacrylate (APA, Darvan 821A, Vanderbilt Minerals, LCC), HNO_3, and deionized water that is mixed at 2000 rpm for 20 s in the planetary mixer. Next, Al_2O_3 (AKP 30, Sumitomo Chemical) and NiO (Sigma) powders were added in a stepwise fashion (≈6 steps) and the ink was mixed at 2000 rpm for 30 s after each addition using the planetary mixer. A thermal initiator, ACPA, was pre-dissolved in water at a 70:30 ratio of water:initiator and, immediately added to the NiO-doped Al_2O_3 ink (held at 5–8 °C) in two steps. The ink was held at 5–8 °C until it was used for printing. The final ink composition contained 69.17 wt% Al_2O_3, 1.48 wt% NiO, 20.36 wt% PEGDA, 0.69 wt% APA, 0.03 wt% HNO_3, 7.78 wt% water, and 0.49 wt% ACPA, which corresponded to a ceramic volume fraction of $\phi \approx 0.395$.

Zeta Potential Measurements: Zeta potential measurements were carried out on dilute suspensions of pure YSZ and PAA-coated YSZ particles ($\phi = 0.01$) as a function of pH using a Zetasizer (Nano-ZS Zen 3600; Malvern). The suspension pH was controlled by adding appropriate amounts of either a 1 M HNO_3 or 1 M NaOH aqueous solution. These measurements were also carried out on dilute Al_2O_3 and APA-coated Al_2O_3 suspensions ($\varphi = 0.01$) following the same procedure (Figure S8, Supporting Information).

Rheological Measurements: The rheological properties of the three colloidal inks and the silicone support matrix were characterized using a rheometer (Discovery HR-3 hybrid rheometer; TA Instruments). Apparent viscosity (η) and moduli (G' and G'') measurements were carried out using a 25 mm diameter disposable parallel plate geometry, in which each plate had 120 grit sandpaper adhered, and were separated by a 300 µm gap. The apparent viscosity was measured as a function of increasing shear rate $\dot{\gamma}$ (from 0.01–100 s^{-1} at 10 points per decade) under direct strain control at 21 °C. The storage (G') and loss (G'') moduli were measured using direct stress control at an oscillation frequency of 1 Hz frequency, as the shear stress was increased from 1 Pa to 10 KPa. The shear yield stress (τ_y) was defined by the crossover point where G' exceeds G''. Complex viscosity (η^*) was measured using a cone-plate geometry with a 40 mm diameter, a 2° cone angle, and a 0.049 mm gap at the tip. Small-amplitude oscillatory shear was used to probe the complex viscosity of the YSZ ink every 6 s (for 60 °C and 70 °C conditions) and every 12 s (for 40 °C and 50 °C conditions) using direct strain control at 10% strain and a frequency of 1 Hz. To prevent solvent evaporation from the ink during the extended measurement period, a small amount of silicone oil (DOWSIL 9040, Dow Silicones) was used to coat the periphery of the cone-plate geometry.

Embedded 3D Printing: The colloidal inks were first warmed to room temperature and then loaded into 10cc syringe barrels (Nordson EFD) prior to mixing at 1900 rpm for 50 s in a planetary mixer to remove any air trapped in the ink. The ink-filled syringe was then placed in a high-pressure dispensing tool (Nordson EFD) and used with an electronic pressure regulator (Ultimus V, Nordson EFD) to achieve printing pressures of up to 700 PSI. Each ink was extruded through 1.5″ long stainless-steel nozzle with either 0.61 mm (20 gauge) or 0.84 mm (18 gauge) inner diameter depending on the desired feature size. The printhead (ink-filled syringe, high-pressure dispenser, and nozzle) was affixed to a custom 3-axis cartesian motion stage (Aerotech Inc., Pittsburg, PA, USA). The electronic pressure regulator was controlled via a serial connection (RS-232) to the motion controller of the stage (A3200, Aerotech Inc.). The sacrificial support matrix was prepared by loading silicone (DOWSIL 9040, Dow Corning) into a cylindrical container (FlackTek). To remove any air from the silicone matrix, this container was centrifuged at 3000 rpm for 3 min, placed under vacuum (−100 kPa) for 2 min, and then centrifuged again at 3000 rpm for 3 min. The silicone matrix-filled container was then placed on the printing stage within a laser-cut acrylic fixture. Toolpaths used to print the octet and cubic lattices were manually designed and generated using parameterized Python scripts. For stochastic lattices, such as the sphere, the structure was first designed in Rhino CAD (McNeel & Associates) then the Automated Eulerian Route Optimization (AERO), a planning algorithm based on graph theory principles, was used to generate the toolpath. For chainmail structures, the toolpath was designed in Fusion 360 (Autodesk), along with a custom plugin utilizing AERO as a backend.

Microwave Irradiation and Thermal Imaging: After EMB3D printing, each printed ceramic architecture along with its silicone support matrix were subjected to microwave irradiation to thermally cure the patterned colloidal ink(s). This process was carried out in a power-controlled microwave oven (Panasonic NE-12521) using a conventional operation frequency of ≈2.45 GHz. Unless otherwise stated, the standard conditions used for microwave irradiation were a power of 360 W applied in irradiation cycles, where each cycle consists of a 30 s pulse followed by a 30 s off interval until sufficient curing has occurred (≈2–6 cycles) (Figure S5, Supporting Information). After curing, the ceramic architectures were physically removed from the silicone matrix and a pressurized air gun was used to remove any residual matrix material. The architectures were then immersed in a paraffin oil bath to dissolve any residual silicone. As a final step, the printed and microwave-cured ceramic architectures were dried in a conventional oven at 60 °C for 24 h. To directly quantify the temperature evolution during microwave irradiation, 2D square lattices (30 × 30 mm) were printed at 2 mm beneath the silicone matrix surface contained in 60 mm × 15 mm round Petri dishes (Sigma-Aldrich). The samples were subjected to varying microwave irradiation conditions, while thermal maps were captured using an infrared camera (FLIR T440) positioned ≈15 cm from the matrix surface. The reported temperature of the lattice was the average temperature of a lattice shaped mask sized to encompass each sample, unless noted otherwise.

Sintering and Microstructural Evolution: All printed, cured, and dried ceramic architectures were sintered by first heating in air to 500 °C followed by a 2 h isothermal hold to remove the polymeric constituents and then heating up to 1500 °C for 2 h using heating and cooling rates of 3 °C min^{-1}. A mixture of carbon, YSZ, and Al_2O_3 particles in a 50:25:25 vol% ratio was used to form a powder bed on which the samples were placed during the sintering process. A field-emission scanning electron microscope (Ultra55 Zeiss) was used to characterize the microstructure of sintered ceramic architectures. To analyze their bulk structure, micro-CT images and videos of these ceramic architectures before and after sintering were obtained using a Versa 620 X-ray microscope (Carl Zeiss, Inc., Pleasanton, CA, USA). Higher and lower magnification tomography images were collected with a microfocus X-ray source with a tube voltage of 140 kV, current of 150 µA, and HE2 source filter. For the lower resolution scans, 4501 projection images were captured for each entire lattice structure on a 16-bit 2048 × 2048 0.4× objective detector with achievable voxel resolutions of 11.26 µm. For the higher resolution scans, 4501 projection images were captured for one representative strut within each lattice structure on a 16-bit 2024 × 20 224 4× objective detector with achievable voxel resolutions of 2.32 µm. Data was reconstructed later using the Zeiss Reconstructor software version 16 (Carl Zeiss, Inc., Pleasanton, CA, USA). 3D data analysis and animations were created using Dragonfly Pro software version 2021.1 (Object Research Systems, Inc., Montréal, Québec, Canada).

Mechanical Properties: Sintered YSZ octet lattices were tested under compression (Instron 5566) at a displacement rate of 1 µm s^{-1}. The top and bottom surfaces of each specimen were polished until they became flat and parallel to ensure a uniform load distribution. A dial indicator (Mitutoyo 3109S-10) mounted to a granite base was used to measure flatness and parallelism. The yield strength (σ_y) was defined by the stress at which 0.2% plastic deformation occurs and the Young's modulus (E) was determined from the slope of the stress-strain curves between 50 and 80% σ_y. The YSZ chain loop structures consisting of 20 round links (link outer diameter ≈10 mm, wire diameter ≈1.75 mm and link weight ≈0.4 g) were subjected to tensile tests. These loop chains were tested under tension (Instron 5566) around two cylindrical stainless-steel posts (12 mm diameter) at a relative displacement rate of $1\ \mu m\ s^{-1}$.

Statistical Analysis: The zeta potential measurements for YSZ and Al_2O_3 were presented as the mean ± standard deviation (SD) for sample size ($n = 3$). Analyses were performed using Origin 8.5 (OriginLab Software).

Supporting Information

Supporting Information is available from the Wiley Online Library or from the author.

Acknowledgements

B.R.-M. and R.D.W. contributed equally to this work. The authors gratefully acknowledge support from the Army Research Office MURI Program (W911NF2120146) and the National Science Foundation under the MRSEC (DMR-2011754). Micro-CT imaging was carried out at the Center for Nanoscale Systems (CNS, Harvard University) with the assistance of G. Lin (CNS) under National Institutes of Health award number S10OD023519. The authors thank L. K. Sanders for assistance with videography and photography and B. Lu for his assistance in the development of the Fusion 360 plugin.

Conflict of Interest

The authors have filed a patent on this work. J.A.L. is a scientific advisor to Desktop Metal, Azul 3D, and Autodesk, Inc.

Author Contributions

B.R.-M., R.D.W., R.L.T., and J.A.L. conceived the project; B.R.-M. and R.D.W. performed research; B.R.-M. and R.D.W. analyzed data; and B.R.-M., R.D.W., and J.A.L. wrote the manuscript.

Data Availability Statement

The data that support the findings of this study are available from the corresponding author upon reasonable request.

Keywords

ceramic lattices, colloidal inks, embedded 3D printing, microwave curing

Received: October 8, 2022
Revised: January 14, 2023
Published online: March 4, 2023

---

[1] N. Travitzky, A. Bonet, B. Dermeik, T. Fey, I. Filbert-Demut, L. Schlier, T. Schlordt, P. Greil, *Adv. Eng. Mater.* **2014**, *16*, 729.
[2] A. Zocca, P. Colombo, C. M. Gomes, J. Günster, *J. Am. Ceram. Soc.* **2015**, *98*, 1983.
[3] J. N. Stuecker, J. E. Miller, R. E. Ferrizz, J. E. Mudd, J. Cesarano, *Ind. Eng. Chem. Res.* **2004**, *43*, 51.
[4] C. Zhu, Z. Qi, V. A. Beck, M. Luneau, J. Lattimer, W. Chen, M. A. Worsley, J. Ye, E. B. Duoss, C. M. Spadaccini, C. M. Friend, J. Biener, *Sci. Adv.* **2018**, *4*, eaas9459.
[5] K. Sun, T.-S. Wei, B. Y. Ahn, J. Y. Seo, S. J. Dillon, J. A. Lewis, *Adv. Mater.* **2013**, *25*, 4539.
[6] C. L. Cramer, E. Ionescu, M. Graczyk-Zajac, A. T. Nelson, Y. Katoh, J. J. Haslam, L. Wondraczek, T. G. Aguirre, S. LeBlanc, H. Wang, M. Masoudi, E. Tegeler, R. Riedel, P. Colombo, M. Minary-Jolandan, *J. Eur. Ceram. Soc.* **2022**, *42*, 3049.
[7] U. Scheithauer, E. Schwarzer, T. Moritz, A. Michaelis, *J. Mater. Eng. Perform.* **2018**, *27*, 14.
[8] J. L. Simon, S. Michna, J. A. Lewis, E. D. Rekow, V. P. Thompson, J. E. Smay, A. Yampolsky, J. R. Parsons, J. L. Ricci, *J. Biomed. Mater. Res., Part A* **2007**, *83A*, 747.
[9] J. L. Ricci, E. A. Clark, A. Murriky, J. E. Smay, *J. Craniofac. Surg.* **2012**, *23*, 304.
[10] S. Bose, S. Vahabzadeh, A. Bandyopadhyay, *Mater. Today* **2013**, *16*, 496.
[11] P. Miranda, E. Saiz, K. Gryn, A. P. Tomsia, *Acta Biomater.* **2006**, *2*, 457.
[12] S. Eqtesadi, A. Motealleh, P. Miranda, A. Pajares, A. Lemos, J. M. F. Ferreira, *J. Eur. Ceram. Soc.* **2014**, *34*, 107.
[13] M. L. Griffith, J. W. Halloran, *J. Am. Ceram. Soc.* **2005**, *79*, 2601.
[14] G. A. Brady, J. W. Halloran, *Rapid Prototyping J.* **1997**, *3*, 61.
[15] C. Hinczewski, S. Corbel, T. Chartier, *J. Eur. Ceram. Soc.* **1998**, *18*, 583.
[16] A. Bertsch, S. Jiguet, P. Renaud, *J. Micromech. Microeng.* **2004**, *14*, 197.
[17] Z. C. Eckel, C. Zhou, J. H. Martin, A. J. Jacobsen, W. B. Carter, T. A. Schaedler, *Science* **2016**, *351*, 58.
[18] F. Kotz, K. Arnold, W. Bauer, D. Schild, N. Keller, K. Sachsenheimer, T. M. Nargang, C. Richter, D. Helmer, B. E. Rapp, *Nature* **2017**, *544*, 337.
[19] N. Kleger, C. Minas, P. Bosshard, I. Mattich, K. Masania, A. R. Studart, *Sci. Rep.* **2021**, *11*, 22316.
[20] J. CesaranoIII, P. D. Calvert, (Sandia Corp), *US6027326A*, **2000**.
[21] J. E. Smay, J. Cesarano, J. A. Lewis, *Langmuir* **2002**, *18*, 5429.
[22] J. E. Smay, G. M. Gratson, R. F. Shepherd, J. CesaranoIII, J. A. Lewis, *Adv. Mater.* **2002**, *14*, 1279.
[23] J. A. Lewis, J. E. Smay, J. Stuecker, J. CesaranoIII, *J. Am. Ceram. Soc.* **2006**, *89*, 3599.
[24] E. Peng, D. Zhang, J. Ding, *Adv. Mater.* **2018**, *30*, 1802404.
[25] E. Feilden, E. G.-T. Blanca, F. Giuliani, E. Saiz, L. Vandeperre, *J. Eur. Ceram. Soc.* **2016**, *36*, 2525.
[26] E. Zanchetta, M. Cattaldo, G. Franchin, M. Schwentenwein, J. Homa, G. Brusatin, P. Colombo, *Adv. Mater.* **2016**, *28*, 370.
[27] J. W. Halloran, *Annu. Rev. Mater. Res.* **2016**, *46*, 19.
[28] C. Sun, X. Zhang, *Sens. Actuators, A* **2002**, *101*, 364.
[29] K. Cai, B. Román-Manso, J. E. Smay, J. Zhou, M. I. Osendi, M. Belmonte, P. Miranzo, *J. Am. Ceram. Soc.* **2012**, *95*, 2660.
[30] B. Y. Ahn, D. Shoji, C. J. Hansen, E. Hong, D. C. Dunand, J. A. Lewis, *Adv. Mater.* **2010**, *22*, 2251.
[31] G. Liu, Y. Zhao, G. Wu, J. Lu, *Sci. Adv.* **2018**, *4*, eaat0641.
[32] J. J. Bowen, S. Mooraj, J. A. Goodman, S. Peng, D. P. Street, B. Roman-Manso, E. C. Davidson, K. L. Martin, L. M. Rueschhoff, S. N. Schiffres, W. Chen, J. A. Lewis, M. B. Dickerson, *Mater. Today* **2022**, *58*, 71.
[33] C. Minas, D. Carnelli, E. Tervoort, A. R. Studart, *Adv. Mater.* **2016**, *28*, 9993.
[34] J. T. Muth, P. G. Dixon, L. Woish, L. J. Gibson, J. A. Lewis, *Proc. Natl. Acad. Sci. USA.* **2017**, *114*, 1832.

[35] B. Román-Manso, J. Muth, L. J. Gibson, W. Ruettinger, J. A. Lewis, *ACS Appl. Mater. Interfaces* **2021**, *13*, 8976.

[36] W. Wu, A. DeConinck, J. A. Lewis, *Adv. Mater.* **2011**, *23*, H178.

[37] M. Wehner, R. L. Truby, D. J. Fitzgerald, B. Mosadegh, G. M. Whitesides, J. A. Lewis, R. J. Wood, *Nature* **2016**, *536*, 451.

[38] M. A. Skylar-Scott, S. G. M. Uzel, L. L. Nam, J. H. Ahrens, R. L. Truby, S. Damaraju, J. A. Lewis, *Sci. Adv.* **2019**, *5*, eaaw2459.

[39] J. T. Muth, D. M. Vogt, R. L. Truby, Y. Mengüç, D. B. Kolesky, R. J. Wood, J. A. Lewis, *Adv. Mater.* **2014**, *26*, 6307.

[40] R. L. Truby, M. Wehner, A. K. Grosskopf, D. M. Vogt, S. G. M. Uzel, R. J. Wood, J. A. Lewis, *Adv. Mater.* **2018**, *30*, 1706383.

[41] M. Mahmoudi, C. Wang, S. Moreno, S. R. Burlison, D. Alatalo, F. Hassanipour, S. E. Smith, M. Naraghi, M. Minary – Jolandan, *ACS Appl. Mater. Interfaces* **2020**, *12*, 31984.

[42] K. Huang, H. Elsayed, G. Franchin, P. Colombo, *Appl. Mater. Today* **2021**, *23*, 101005.

[43] R. Hoogenboom, U. S. Schubert, F. Wiesbrock, *Microwave-Assisted Polymer Synthesis*, Springer International Publishing, Cham, Switzerland, **2016**.

[44] C. Ebner, T. Bodner, F. Stelzer, F. Wiesbrock, *Macromol. Rapid Commun.* **2011**, *32*, 254.

[45] R. D. Weeks, R. L. Truby, S. G. M. Uzel, J. A. Lewis, *Adv. Mater.* **2022**, *35*, 2206958.

[46] R. C. Chiu, T. J. Garino, M. J. Cima, *J. Am. Ceram. Soc.* **1993**, *76*, 2257.

[47] T. M. Shaw, *Phys. Rev. Lett.* **1987**, *59*, 1671.

[48] Y. Zhou, Z. Zhang, A. Postma, G. Moad, *Polym. Chem.* **2019**, *10*, 3284.

[49] L. J. Gibson, M. F. Ashby, *Cellular Solids: Structure and Properties*, Cambridge University Press, Cambridge, UK, **2001**.

[50] Y. Wang, L. Li, D. Hofmann, J. E. Andrade, C. Daraio, *Nature* **2021**, *596*, 238.